Rheol Acta
DOI 10.1007/s00397-011-0539-0

ORIGINAL CONTRIBUTION

Non-linear dynamics of semi-dilute polydisperse polymer solutions in microfluidics: effects of flow geometry

Zhuo Li · Xue-Feng Yuan · Simon J. Haward · Jeffrey A. Odell · Stephen Yeates

Received: 30 June 2010 / Revised: 2 January 2011 / Accepted: 25 February 2011

Abstract The non-linear dynamics of a semi-dilute ($c/c^* = 15$) polydisperse polyethylene oxide (PEO) solution in microfluidics are studied experimentally using benchmark contraction–expansion flow geometries with three contraction–expansion ratios (4:1:4, 8:1:8 and 16:1:16) and two narrow channel lengths ($L_c/D_h = 53$ and 5.3, where L_c is the length of the narrow channel and D_h is its hydraulic diameter). Complex flows over a range of elasticity numbers (El), Weissenberg numbers (Wi) and Reynolds numbers (Re) are characterized using micro-particle image velocimetry (μ-PIV) and pressure drop measurements. The evolution of vortex formation and dynamics has been visualized through a step-flow-rate experiment. Various flow dynamics regimes have been quantified and are presented in a Wi–Re diagram. The experimental results reveal that the contraction ratio can result in qualitatively different vortex dynamics of semi-dilute polymer solutions in microfluidics, whereas the length of the narrow channel merely affects the dynamics at a quantitative level. A single elasticity number, if defined by the size of the narrow channel, is not sufficient to account for the effects of contraction ratio on the non-linear vortex dynamics.

Keywords Semi-dilute polymer solution · Contraction flow · PIV · Viscoelastic fluid · Elongational flow · Pressure drop

Z. Li · X.-F. Yuan (✉)
Manchester Interdisciplinary Biocentre and School of Chemical Engineering and Analytical Science, University of Manchester, 131 Princess Street, Manchester, M1 7DN, UK
e-mail: xue-feng.yuan@manchester.ac.uk

S. J. Haward · J. A. Odell
HH Wills Physics Laboratory, The University of Bristol, Tyndall Avenue, Bristol, BS8 1TL, UK

S. Yeates
School of Chemistry, The University of Manchester, Oxford Road, Manchester, M13 9PL, UK

Introduction

The abrupt contraction is a benchmark flow geometry commonly used to study non-linear dynamics of complex fluids in both macroscale geometries (Cogswell 1972; Williams and Williams 1985; Binding and Walters 1988) and, more recently, microscale geometries (James and Saringer 1982; Groisman et al. 2003; Rodd et al. 2005, 2007; Gulati et al. 2008). The flow phenomena of viscoelastic fluids in macroscale entry flow have been studied by a large number of experiments including axisymmetric geometries (Cable and Boger 1978a, b, 1979; Rothstein and McKinley 1999, 2001), planar geometries (Evans and Walters 1986, 1989; White and Baird 1988; Boger 1987; Quinzani et al. 1994, 1995; Nigen and Walters 2002; Alves et al. 2005) and by numerical simulations (Baloch et al. 1996; Purnode and Crochet 1996; Xue et al. 1998; Alves et al. 2000, 2004; Aboubacar et al. 2002; Omowunmi and Yuan 2010).

The earlier studies concentrate on characterizing flow pattern of various viscoelastic fluids in macroscale axisymmetric or planar contraction flows over a wide range of contraction ratios. The experimental works

Published online: 01 April 2011

(Cogswell 1972; Cable and Boger 1978a; Boger 1987; McKinley et al. 1991) revealed the importance of the extensional viscosity of fluids in determining vortex size. The ratio of extensional and shear flow properties at steady state can be used as a measure in determining vortex growth mechanism (Binding 1988), and the presence or absence of vortex growth (White and Baird 1988). By using the birefringence measurements, Quinzani et al. (1994, 1995) found that the extensional viscosity of polymer solution exhibited slight thickening followed by apparent thinning with increasing flow rate. This thinning phenomenon was attributed to the decrease of the residence time of the polymer molecules in the high-strain-rate region near the contraction throat. The experimental data can be fitted by Phan-Thien-Tanner model. The transient behaviour of both extensional and shear stresses were also considered by Rothstein and McKinley (2001). For shear-thinning fluid the size of the salient corner vortex formed in the axisymmetric contraction was smaller than that of the planar case. This was attributed to the reduced total Hencky strain in the planar contraction throat. The numerical results of Purnode and Crochet (1996) reveal a lip vortex mechanism in flow of large contraction ratios with negligible inertial effects. The authors pointed out that the steady-state extensional flow properties of the fluid cannot fully account for the different vortex dynamics, because solutions with different polymer concentrations show similar trends in extensional viscosity with extensional strain rate. This view is also consistent with the later numerical work by Xue et al. (1998).

Pressure drop across the upstream and downstream regions is another important quantity for non-linear flow characterisation. Earlier experiments in axisymmetric contractions showed a substantial extra pressure drop in polymer solutions, well above the value obtained for a Newtonian fluid with equal viscosity at the same flow rate (Rothstein and McKinley 1999, 2001; Nigen and Walters 2002; Binding 1988). However, in planar contraction flows, no difference in the pressure drop was observed between a Boger fluid and a Newtonian fluid with the same shear viscosity (Nigen and Walters 2002). Quantitative characterisation of the pressure drop in complex flow geometry is of significant to the extraction of the rheometric properties of polymer solutions and still remains elusive.

By utilizing micro-fabricated geometries, a wide viscoelastic flow regime can be readily accessed, in particular much higher Weissenberg number (Wi) and moderate Reynolds number (Re) regime, which has not been explored by the macroscale experiments. The recent studies (Rodd et al. 2005, 2007; Gulati et al. 2008; Li et al. 2011) begin to map out highly non-linear dynamic behaviour of polymer solutions in very shallow flow geometry in term of Wi and Re by varying the rheological properties of fluids and using a fixed flow geometry, respectively. The variation of pressure drop with Wi is closely correlated to different flow regime. Using a multi-mode PPT model, recent 3-D computer simulation results on the flow of semi-dilute polymer solutions through 8:1 planar contraction (Omowunmi and Yuan 2010) show that varying the aspect ratio of a planar contraction, defined as the ratio of the depth to the upstream width of the flow channel, can have a similar effect to varying fluid properties so as to modify the elasticity number of the flow. There is no lip vortex for contraction entry flow with a high aspect ratio or approximately 2-D flow geometry.

The underlying physical mechanism for vortex growth or suppression depends on fluid rheological properties and flow geometry. There is no experimental work to systematically investigate the effects of the flow geometry on non-linear dynamics of polymer solutions in shallow flow geometry. In this paper, the non-linear dynamics of a well characterized 0.3 wt.% semi-dilute ($c/c^* = 15$) PEO solution in various shallow flow geometries will be reported. By using micro-particle image velocimetry (μ-PIV) and transient pressure drop measurements, non-linear dynamics of the polymer solution are investigated over wide ranges of Wi ($3 < Wi < 120$) and Re ($0.05 < Re < 4.3$), and in five flow geometries including three contraction–expansion ratios of 4:1:4, 8:1:8 and 16:1:16, and two narrow channel lengths L_c ($L_c/D_h = 53$ and 5.3, where D_h is the hydraulic diameter of the narrow channel) under the same 8:1:8 contraction–expansion ratio. In Section "Experimental techniques", experimental techniques are briefly presented. Experimental results and discussion follow in Section "Results and discussion". Various flow regimes along El lines are classified in a Wi–Re diagram. The evolution of flow patterns are analyzed and correlated with the pressure drop measurements. Conclusions are given in Section "Conclusions".

Experimental techniques

Materials and molecular characterization

PEO sample is a pharmaceutical grade sample (POLYOX™ WSR N-60K) kindly supplied by Dow Chemicals. 0.3 wt.% PEO aqueous solutions were prepared by dissolving PEO powder in de-ionized water. The solutions were stored in a refrigerator at 4°C for about 7 days, with occasional and gentle shaking by hand to allow complete dissolution of PEO whilst

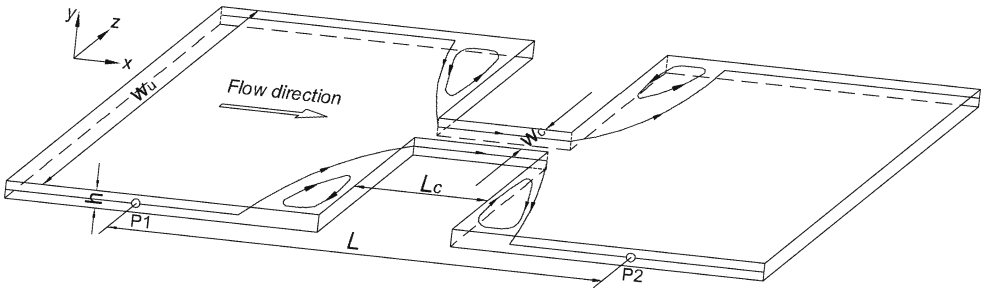

Fig. 1 Schematic diagram of a planar contraction–expansion geometry including definitions of important length scales. The entrance of the contraction throat is located as the origin ($x = 0$, $y = 0$, $z = 0$)

avoiding mechanical degradation. Only freshly made PEO aqueous solutions were used in each experiment reported hereafter. The molecular weights and molecular weight distribution of the PEO sample were characterized using standard Gel Permeation Chromatography (GPC) with TSK PW 5000 and 6000 columns, an ERC 751A differential refractometer and a Waters 510 pump, and an aqueous solvent.

Rheometry

The rheometric properties of the PEO solution were measured using a range of experimental techniques, including an ARES rotational shear rheometer (TA Instruments) with a double wall Couette geometry (cup OD = 34 mm, cup ID = 27.95 mm, bob OD = 32 mm, bob ID = 29.5 mm), a Vilastic-3 Viscoelasticity Analyzer (Vilastic Scientific Inc.), a CaBER capillary breakup extensional rheometer (Thermo Fisher Scientific). The characteristic relaxation time (λ) and surface tension (κ) of the solution were measured using CaBER and CIR100 Interfacial Rheometers (Camtel Ltd), respectively.

Micro-channel geometry

The micro-channels are made of poly(methyl methacrylate) and aromatic epoxy, and were fabricated by standard soft lithographic method (Epigem Ltd, the UK). The internal surfaces were treated by oxygen plasma to make them hydrophilic. Figure 1 shows a schematic diagram. Table 1 summarizes all the dimensions of micro-channels (Nos. 1–5), including upstream channel width w_u, downstream contraction width w_c, downstream length L_c, uniform depth h, the hydraulic diameter D_h ($D_h = 2w_c h/(w_c + h)$), contraction–expansion ratio β ($\beta = w_u/w_c$), channel aspect ratio α ($\alpha = w_u/h$), and Hencky strain ε_H. The total Hencky strain experienced by a fluid element can be approximated as $\varepsilon_H = ln(w_u/w_c)$. The downstream width ($w_c$) was chosen to be the characteristic length of each flow geometry to calculate the dimensionless numbers *Re*, *Wi* and *El*.

Differential pressure sensors (Linkam Scientific Instrument Ltd.) were integrated into these flow cells at the position P_1 and P_2 (see Fig. 1) to measure the pressure drop ΔP_{12}. For all Nos. 1–5 micro-channels, the pressure taps were fixed far away from the reentrant region to avoid the vortex disturbance. A syringe pump (Chemyx Nexus 5000) was used to drive the fluid flow to achieve a range of volumetric flow rates (Q), within which the measured pressure drops are smooth and the pulsation effects are negligibly small in comparison with the pressure readings.

Micro-particle image velocimetry

A micro-particle image velocimeter (TSI Instrument Ltd) was used to measure the 2-D velocity field at the centreplane ($x - z$) of the flow channel, as used in our previous work (Haward et al. 2010a, b; Li et al. 2011). Standard Nikon ×10 objective lens ($NA = 0.3$) and ×20 objective lens ($NA = 0.45$) were used. PEO solutions were seeded with Epi-fluorescent particles (particle diameter $d_p = 1.0$ μm, $Ex_{max.}/Em_{max.}$ = 542/612 nm, Duke) by the weight concentrations 0.01 and 0.02 wt.% for $M \times NA = 10 \times 0.3$ and 20×0.45, respectively. For this μ-PIV system setting, the estimated measurement depth is 26 μm if using ×10 ($NA = 0.3$) lens or 12 μm

Table 1 Dimensions of five micro-channels

Micro-channel no.	Contraction-expansion ratio	w_u (μm)	w_c (μm)	L (mm)	L_c (mm)	h (μm)	D_h (μm)	L_c/D_h	α	ε_H
1	4:1:4	800	200	40	20	45	73.5	272	17.8	1.4
2	8:1:8	800	102	40	20	45	62.5	320	17.8	2.1
3	16:1:16	400	25	40	20	45	32.1	623	8.9	2.8
4	8:1:8	800	100	12	4	61	75.8	53	13.1	2.1
5	8:1:8	800	100	10	0.4	61	75.8	5.3	13.1	2.1

if using $\times 20$ ($NA = 0.45$) lens. These depths of field are equivalent to 58% or 27% of the channel depth ($h = 45$ μm), respectively. The error in the velocity measurements is about 12∼16% below the true value.

Results and discussion

Molecular and rheological characterization

The GPC results are shown in Fig. 2. The mean radius of gyration (R_g) of PEO molecules was estimated from $< R_g > = 0.215 M_w^{0.583 \pm 0.031}$ (Å) proposed by Devanand and Selser (1991). The overlap concentrations c^* are calculated by assuming a simple cubic packing of PEO molecules, i.e. $c^* = M_w / \left[N_A \left(2R_g \right)^3 \right]$ (N_A is Avogadro's constant). Note that the estimation of the c^* value based on the simple cubic packing assumption is about half of the value estimated by Rodd et al. (2005), who used the closest sphere packing assumption. Accordingly, 0.3 wt.% PEO solution is in the semi-dilute regime ($c/c^* = 15$). The viscosity data obtained from ARES and Vilastic-3 are presented in Fig. 3 and shown a good agreement between these two techniques. The key data of the molecular and rheometric characterization are listed in Table 2. The comprehensive rheometric results can be found in Li et al. (2011).

Evolution of vortex dynamics

In order to study the effects of the contraction ratio on the evolution of vortex formation and dynamics of PEO solution, flow images were captured in the upstream zone of various contraction ratio flow by μ-PIV over a period of several seconds following a step change of flow rate. Figure 4 displays the transient flow behaviour

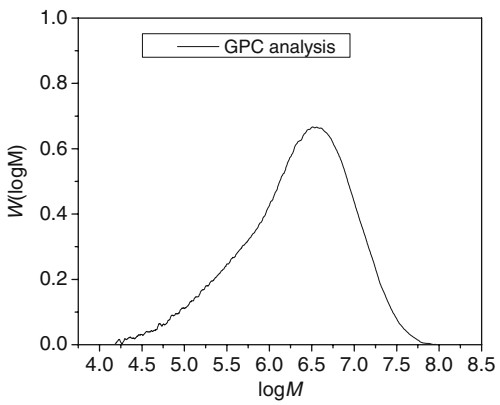

Fig. 2 Molecular weight distribution of PEO measured by GPC

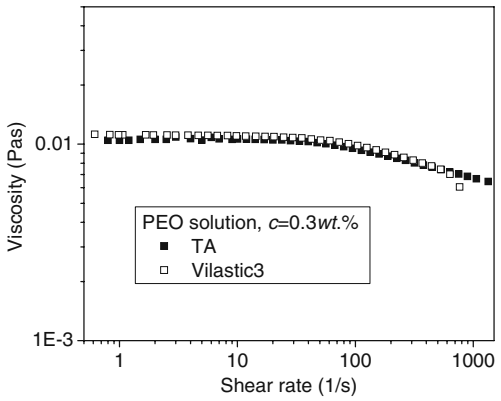

Fig. 3 Shear viscosity of 0.3 wt.% PEO solution measured by ARES and Vilastic-3 at 25°C

of the 0.3 wt.% PEO solution in the 4:1 contraction (left-hand column), 8:1 contraction (middle column) and 16:1 contraction (right-hand column).

In the 4:1 contraction flow, the images were captured after a step change of flow rate from 9.5 ml/h ($Re = 2.04$, $Wi = 17.6$) to 10 ml/h ($Re = 2.15$, $Wi = 18.5$) at $t = 0$ s, here inflecting streamlines are a signature of the viscoelastic effect becoming significant. At $t = 0.25$ s, a small vortex appears at the left salient corner. Then, it climbs along the channel surface and develops into a corner vortex as shown in the images at $t = 0.5$ s and 0.75 s. In the steady state, symmetric vortex appears as shown at $t = 5.25$ s.

In the 8:1 contraction flow, the images were captured after a step change of flow rate from $Q = 3.5$ ml/h ($Re = 1.25$, $Wi = 24.9$) to $Q = 4.5$ ml/h ($Re = 1.6$, $Wi = 32.0$). In the initial state ($t = 0$ s), the appearance of inflections in the streamlines due to elastic effects is evident. A bistable asymmetric lip vortex appears at $t = 0.25$ s, followed by symmetric lip vortices

Table 2 The properties of 0.3 wt.% PEO aqueous solution at $T = 25$°C and a range of the dimensionless number flows studied

c (wt.%)	0.3
M_w (g/mol)	4.82×10^6
M_w/M_n	7.5
ρ (kg/m^3)	991
R_g (nm)	169.2
c^* (wt.%)	0.0206
c/c^*	15
η_0 (mPa·s)	10.5
κ (mN/M)	60.7
λ_{CaBER} (ms)	6
$< \dot{\gamma} > = 2\langle V \rangle / w_c$ (1/s)	593–23,703
$Re = \rho \langle V \rangle D_h / \eta_0 = 2\rho Q / (w_c + h)\eta_0$	0.075–5.4
$Wi = \lambda \dot{\gamma}_c = 2\lambda \langle V \rangle / w_c = 2\lambda Q / h w_c^2$	3.5–142
$El = Wi/Re = \lambda \eta (w_c + h) / \rho w_c^2 h$	8.6, 16.7, 20, 158

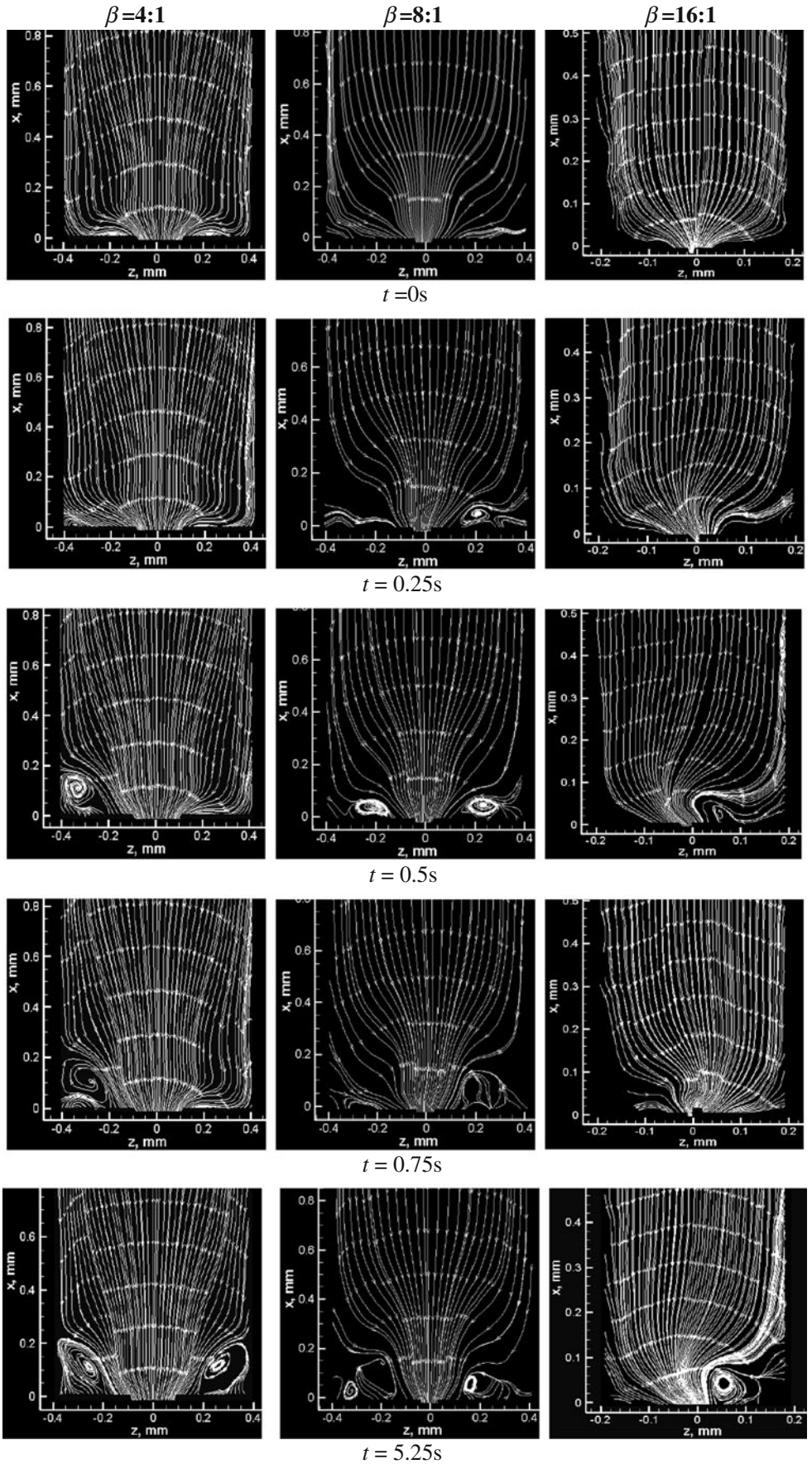

Fig. 4 Transient flow pattern of 0.3 wt.% PEO solution in the micro-channels (Nos. 1–3). The images in left-hand column are for contraction $\beta = 4{:}1$ after a step change of flow rate from 9.5 ($Re = 2.04$, $Wi = 17.6$) to 10 ml/h ($Re = 2.15$, $Wi = 18.5$). The images of middle column are for contraction $\beta = 8{:}1$ after a step change of flow rate from 3.5 ($Re = 1.25$, $Wi = 24.9$) to 4.5 ml/h ($Re = 1.6$, $Wi = 32.0$). The images of right-hand column are for contraction $\beta = 16{:}1$ after a step change of flow rate from 0.1 ml/h ($Re = 0.08$, $Wi = 11.9$) to 0.3 ml/h ($Re = 0.23$, $Wi = 35.6$)

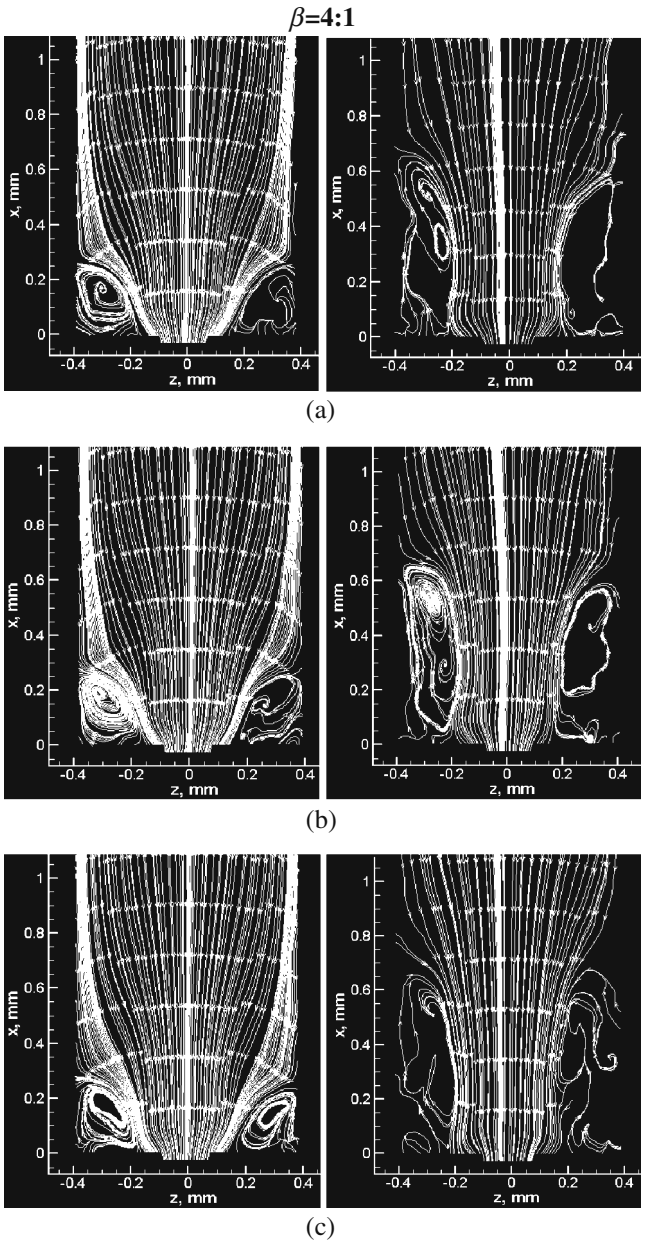

Fig. 5 Transient flow pattern of 0.3 wt.% PEO solution in the 4:1 contraction micro-channel (No.1 and $El = 8.6$) at **a** $t = 0$ s, **b** $t = 0.25$ s and **c** $t = 0.5$ s, under two flow rates, $Q = 11$ ml/h, $Re = 2.36$, $Wi = 20.4$ (the *left-hand column* images) and $Q = 20$ ml/h, $Re = 4.30$, $Wi = 37$ (the *right-hand column* images), respectively

at $t = 0.5$ s and lip vortex growth at $t = 0.75$ s. At $t = 1.0$ s, the lip vortex grows into an unstable corner vortex. Then, the vortex spreads toward the stagnant corner. At $t = 5.25$ s, the radial location of the vortex centre saturates and the large elastic corner vortex appears and starts to grow upstream. The vortex evolution mechanism in the 8:1 contraction flow is different from the one in the 4:1 contraction flow.

In the 16:1 contraction flow, the images were captured after a step change of flow rate from 0.1 ml/h ($Re = 0.08$, $Wi = 11.9$) to 0.3 ml/h ($Re = 0.23$, $Wi = 35.6$). At $t = 0$ s, a weak viscoelastic effect is observed in a form of the gently inflecting streamlines. At $t = 0.25$ s, the viscoelastic effect is shown as the streamlines inflecting asymmetrically. At $t = 0.5$ s, a strongly asymmetric lip vortex appears. At $t = 0.75$ s, the inflecting

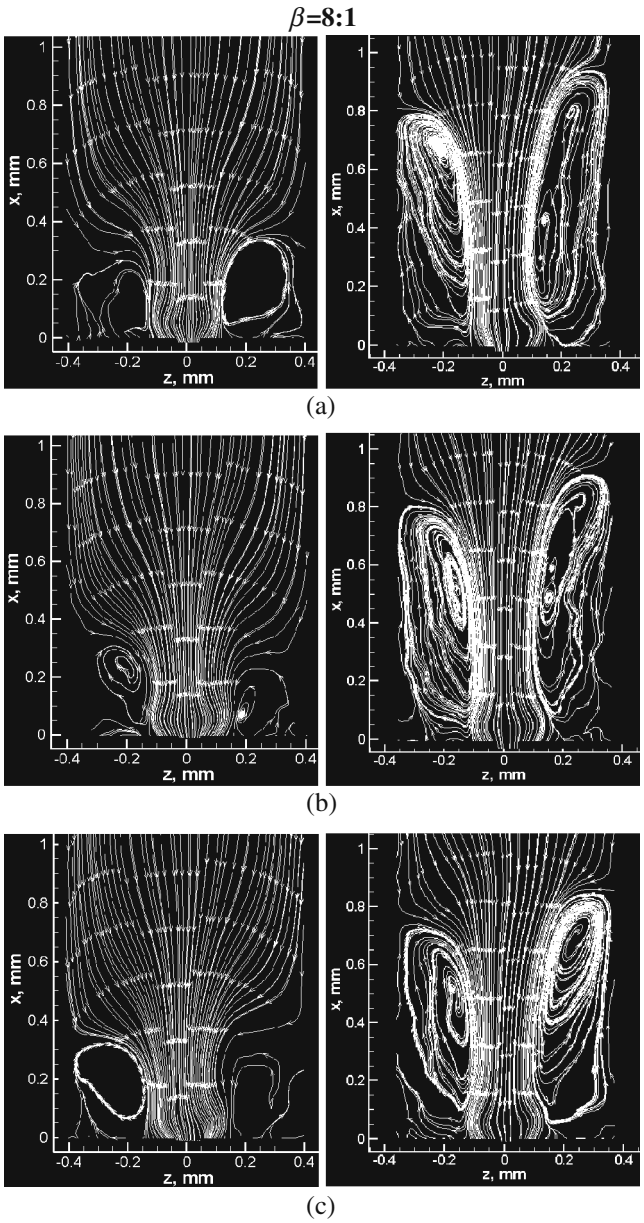

Fig. 6 Transient flow pattern of 0.3 wt.% PEO solution in the 8:1 contraction micro-channel (No. 2 and $El = 20$) at **a** $t = 0$ s, **b** $t = 0.25$ s and **c** $t = 0.5$ s, under two flow rates, $Q = 6$ ml/h, $Re = 2.1$, $Wi = 42.7$ (the *left-hand column* images) and $Q = 10$ ml/h, $Re = 3.6$, $Wi = 71$ (the *right-hand column* images), respectively

streamlines switch from the right side to the left side of the contraction entrance. At $t = 5.25$ s, the lip vortex begins to grow in size. The overall vortex evolution in the upstream channel is very different from in the 4:1 contraction flow. The vortex evolution is brought about by the lip vortex in the 8:1 and 16:1 contraction flow, whereas in the 4:1 contraction flow, the vortex evolution initiates from the vortex close to the channel surface.

Effect of contraction ratio on flow pattern

The time-dependent flow patterns of the 0.3 wt.% PEO solution in the upstream section of micro-channels Nos. 1–3 with contraction ratios 4:1, 8:1 and 16:1 at $t = 0, 0.25$ and 0.5 s are presented in Figs. 5, 6 and 7. All these images were captured sequentially after the pressure drop had reached a steady state. Figure 5 displays the results of the 4:1 contraction flow at two flow

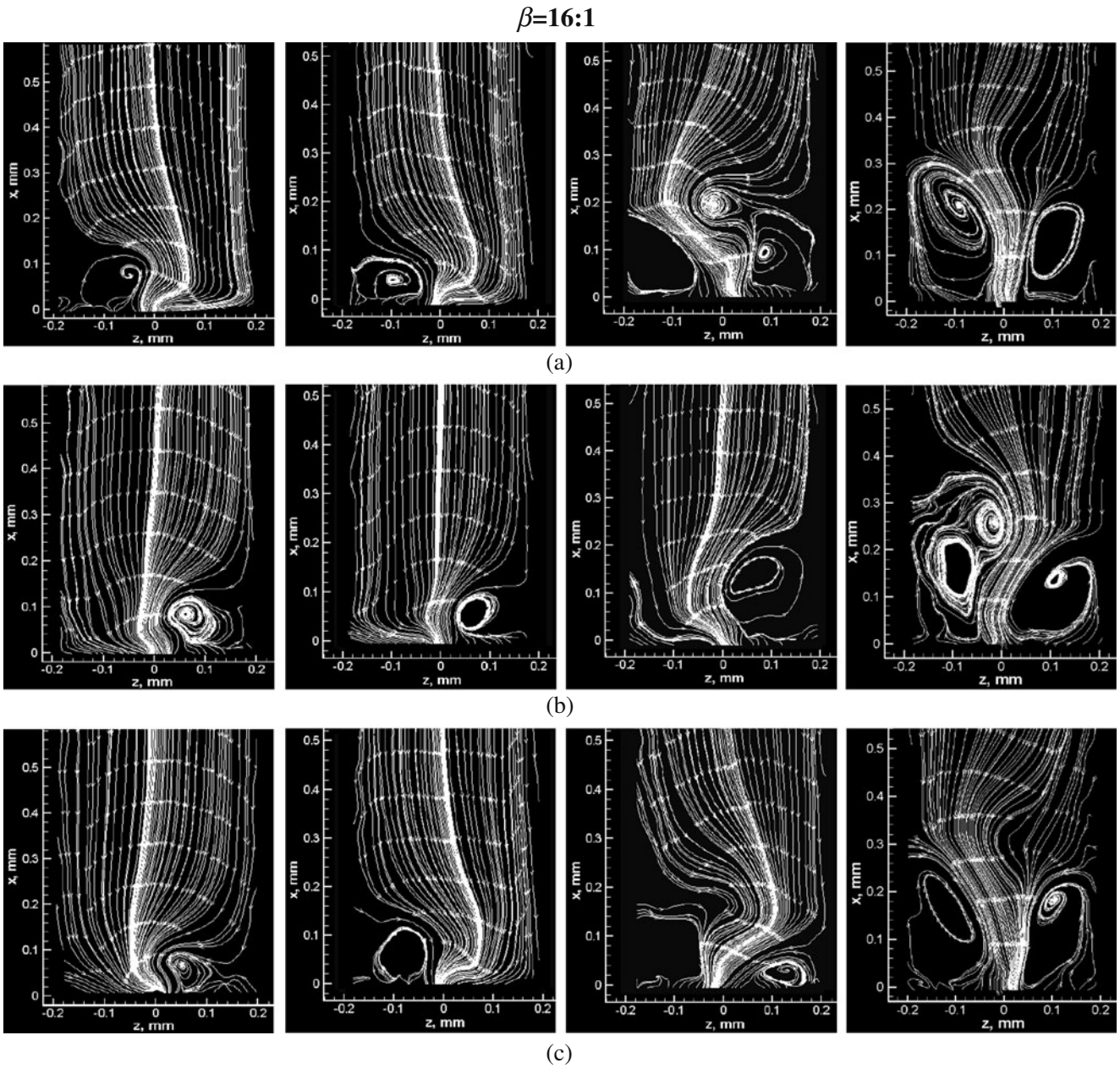

Fig. 7 Transient flow patterns of 0.3 wt.% PEO solution in the 16:1 contraction micro-channel (No. 3 and $El = 158$) at **a** $t = 0$ s, **b** $t = 0.25$ s and **c** $t = 0.5$ s, under four flow rates. From the *left-hand*, the *first column* images are for $Q = 0.4$ ml/h ($Re = 0.30$, $Wi = 47.4$), the *second column* for $Q = 0.6$ ml/h ($Re = 0.45$, $Wi = 71.1$), the *third* for $Q = 0.9$ ml/h ($Re = 0.68$, $Wi = 107$) and the *fourth column* are for $Q = 1.1$ ml/h ($Re = 0.83$, $Wi = 130.4$)

rates: the left-hand column images show $Q = 11$ ml/h, $Re = 2.36$, $Wi = 20.4$ and the right-hand column images show $Q = 20$ ml/h, $Re = 4.30$, $Wi = 37$. The corner vortex size increases as increasing flow rate and remains stable and symmetric. These results are consistent with what observed by Gulati et al. (2008) in the 2:1 contraction flow, in which all vortices were symmetric about the centreline and stable. No lip vortex was observed in the 4:1 contraction even at high Weissenberg numbers ($Wi \sim 209.6$). In the 8:1 contraction flow, as shown in Fig. 6, the vortex structure and size become time-dependent at relatively low flow rates ($Q = 6$ ml/h, $Re = 2.1$, $Wi = 42.7$ and $Q = 10$ ml/h, $Re = 3.6$, $Wi = 71$). The vortex is not only switching from left to right but also moving up and down. In the 16:1 contraction flow, as shown in Fig. 7, the vortex structures are dramatically asymmetric, in significant contrast from the observations made in the 4:1 and 8:1 contractions. At flow rates of $Q = 0.9$ ml/h ($Re = 0.68$, $Wi = 107$) and 1.1 ml/h ($Re = 0.83$, $Wi = 130.4$), two coexisting vortices were observed on one side of the upstream channel. This phenomenon has never been reported in the literature. Obviously, the contraction ratio determines the total Hencky strain imposed on the fluids and plays an important role in the vortex dynamics. The extensional deformation experienced by the PEO solution will be quantitatively analyzed in Section "Velocity measurement and evaluation of local extensional deformation rate".

The flow patterns of PEO solutions in different contraction ratios but at similar El are compared in Fig. 8. The left-hand column images are from 0.45 wt.% PEO solution ($\eta_0 = 22.5$ mPa s, $c/c^* = 22.5$) in the 8:1 contraction micro-channel (No. 2) and $El = 120$ (Li et al. 2011). The right column images are from the 0.3 wt.% PEO solution in the 16:1 contraction micro-channel (No. 3) and $El = 157$. The images in each row are compared at roughly equal Re and Wi. In contrast to the asymmetric patterns of the 16:1 contraction flow, both the lip and corner vortices are symmetric in the 8:1 contraction flow. It is clear that the elasticity number alone, conventionally defined by the length scale of the narrow channel, cannot completely account for the effects of the contraction ratio.

The non-linear dynamics of the 0.3 wt.% PEO solution in the three micro-channels (Nos. 1–3) can be summarized in a Wi–Re diagram, as shown in Fig. 9, in term of the elasticity number ($El = 8.6$, 20 and 158) and the contraction ratio ($\beta = 4{:}1$, 8:1 and 16:1). For all the contraction ratios, the flow pattern changes from Newtonian-like to steady viscoelastic flow with bending streamlines as flow rate increases. In the 4:1 contraction flow, the viscoelastic effect emerges at $Re = 0.86$, $Wi =$

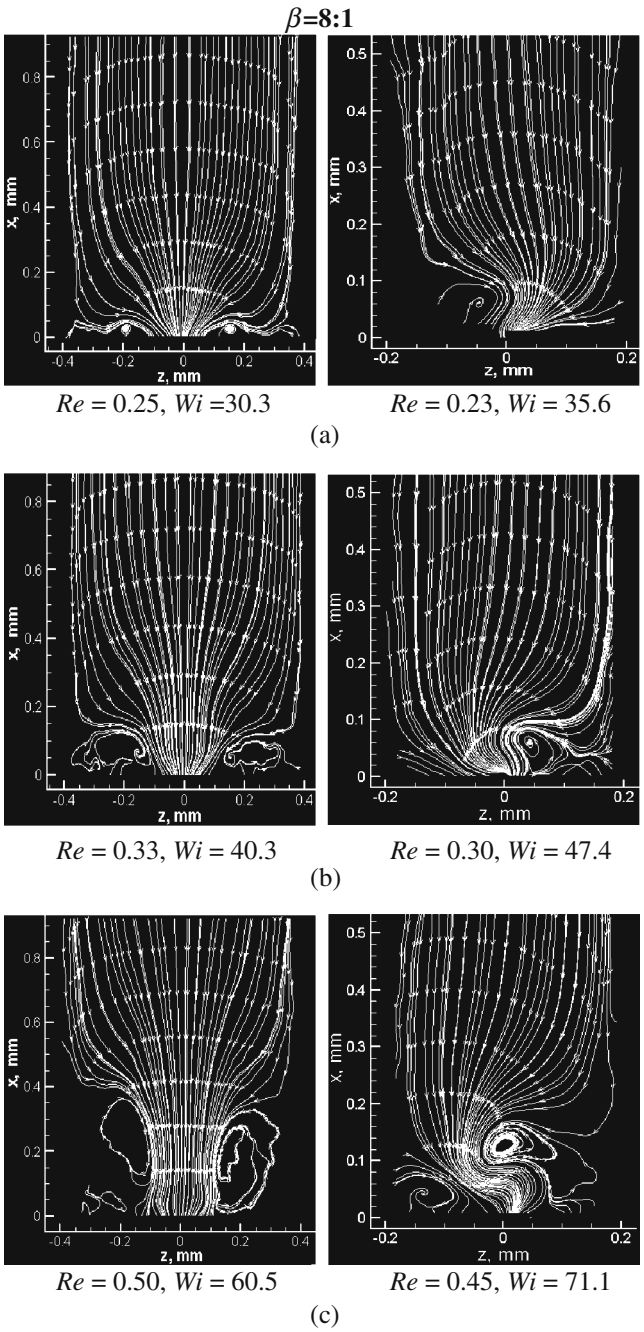

Fig. 8 Flow pattern of PEO solutions: the left-hand column images are from 0.45 wt.% PEO solution flow in the 8:1 contraction micro-channel (No. 2 and $El = 120$); the *right-hand column* images are from 0.3 wt.% PEO solution flow in the 16:1 contraction micro-channel (No. 3 and $El = 158$)

7.4. Symmetric and stable corner vortices are formed in steady-state flow at $Wi = 18.5$, $Re = 2.1$, and there is no lip vortex. However, a lip vortex is observed in the 8:1 contraction flow at $Wi \sim 28.5$ and in the 16:1 contraction flow at $Wi \sim 32$. On further increase of flow rate, the corner vortex replaces the lip vortex but

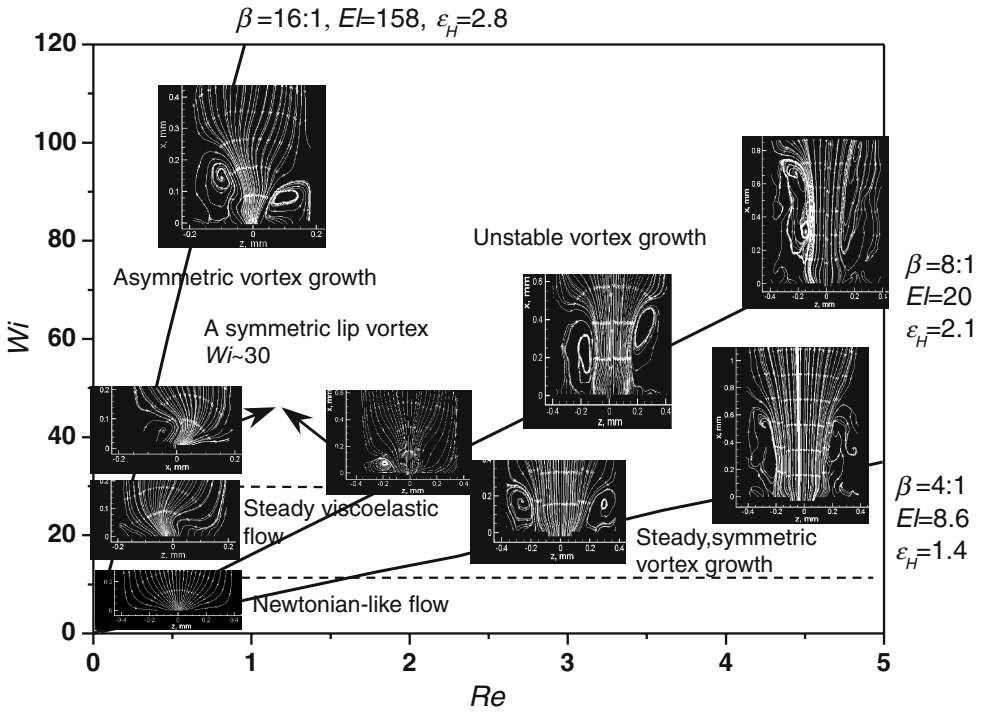

Fig. 9 Summary of flow regimes in *Wi*–*Re* space for 0.3 wt.% PEO solution flow in the micro-channels (Nos. 1–3) with the contraction ratio $\beta = 4{:}1$, 8:1 and 16:1

is much less symmetric and less stable than the corner vortex in the 4:1 contraction flow. The vortices in the 16:1 contraction flow are even more asymmetric and unstable in higher *Wi* flow ($Wi > 32$). The contraction ratio is a sensitive geometric parameter in classification of flow regime.

Velocity measurement and evaluation of local extensional deformation rate

The velocity profiles of the 0.3 wt.% PEO solution in the upstream channel of the 16:1 contraction flow for a flow rate ($Q = 0.1$ ml/h, $Re = 0.08$ and $Wi = 11.9$) at $x = 0.4, 0.2, 0.1$ and 0.05 mm are presented in Fig. 10a, b. They were obtained by averaging over a sequence of 30 pairs of μ-PIV images captured by using objective lens $M\times\ NA = 20 \times 0.45$. All velocities were normalised by the average flow speed in the narrow channel, i.e. $<V> = Q/(w_c \cdot h)$. On the upstream side there is a fully developed velocity profile ($x = 0.4$ mm from the contraction throat). Approaching the contraction throat ($x = 0.2$ mm), the profile near the centre begins to protrude slightly. This is much more pronounced close to the throat (e.g. $x = 0.1$ and 0.05 mm). The velocity profiles are symmetric at all positions. No statistically significant wall-slip effects (within the measurement error) were identified.

Under higher flow rate, the velocity data were extracted from an instantaneous velocity field after the pressure drop had reached steady state. Although in general the flow of the 0.3 wt.% PEO solution in the 16:1 contraction is unstable and time-dependent, under most flow rates in the 4:1 and 8:1 contractions the maximum sideways displacement of the fluid core from the centreline ($y = 0$, $z = 0$) is less than 25% of w_c, and the streamline bunch close to the flow axis is nearly symmetric. The profile of extensional rate can be readily calculated from the centreline velocity to reveal the deformation history undergone by PEO molecules flowing along the centreline and to provide some physical insight to the non-linear fluid dynamics.

In the 4:1 contraction flow, Fig. 11a shows that the axial velocity profile at the flow rate $Q = 2$ ml/h ($Wi = 3.7$) overlaps with the result of water and the centreline velocity increases monotonically towards the contraction throat. At the flow rate $Q = 6$ ml/h ($Wi = 11.1$), the velocity profile starts to depart from the Newtonian-like flow and the region of fluid acceleration extends towards the upstream area. At the flow rate $Q = 10$ ml/h ($Wi = 18.5$), the vortex begins to appear and the velocity curve starts to inflect at $x/w_c = 0.25$ approaching towards the contraction throat. The vortex grows with increasing flow rate. At the flow rate $Q = 20$ ml/h ($Wi = 37$), the axial velocity profile

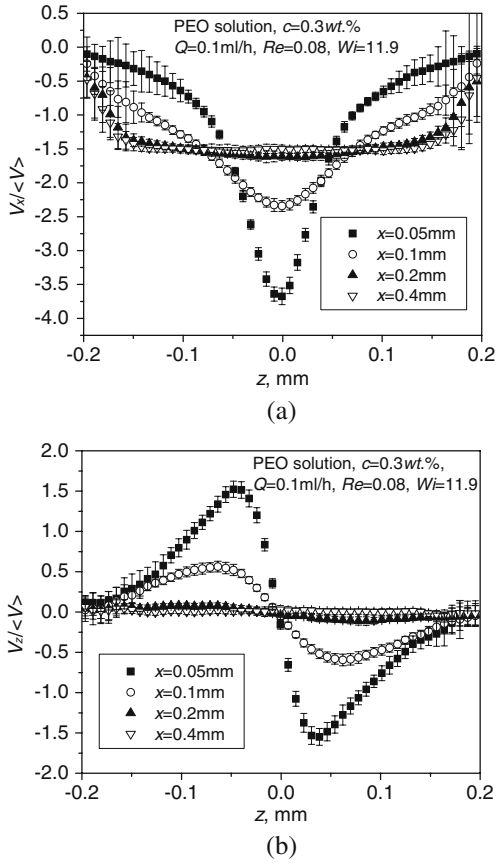

Fig. 10 Dimensionless steady-state velocity profiles of the 0.3 wt.% PEO solution at $x = 0.4, 0.2, 0.1$ and 0.05 mm in the upstream micro-channel of the 16:1 contraction flow (No. 3) at $Q = 0.1$ ml/h ($Re = 0.08$ and $Wi = 11.9$, Newtonian-like flow regime): **a** $V_x/ < V >$ and **b** $V_z/ < V >$

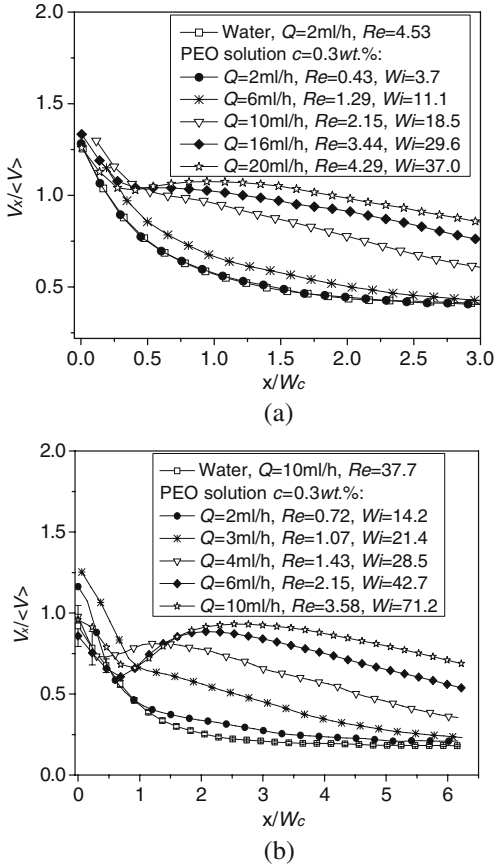

Fig. 11 Axial dimensionless velocity profiles for PEO solution ($c = 0.3$ wt.%) and water flow in the upstream of micro-channels (Nos. 1 and 2) at various flow rates: **a** $\beta = 4{:}1$ and **b** $\beta = 8{:}1$

exhibits a minimum at a position around $x/w_c = 0.4$. Similar trends are also observed in Fig. 11b for the 0.3 wt.% PEO solution flow in the 8:1 contraction, but more pronounced.

The profile of extensional rate can be readily calculated from the centerline velocity and is shown in Fig. 12. The extensional deformation rates along the centreline in the 4:1 contraction flow are compared with those in the 8:1 contraction flow. At low flow rates ($Wi \sim 20$), there is not much difference between the extensional rate profile in these two contraction flows. Further increasing flow rate, the lip vortex (which only occurs in the 8:1 contraction flow) and corner vortex regimes eventually occur. The non-linear flow phenomena couple with the appearance of a compression valley and an extensional peak in the extensional rate profile. The position of the valley and the peak shift toward the upstream area as flow rate is increased. PEO chains are first subjected to compression and then to strong extensional deformation. Under similar Wi numbers, much higher volume flow rate in the 4:1 contraction flow results in its the local extensional rate significantly higher than those in the 8:1 contraction flow.

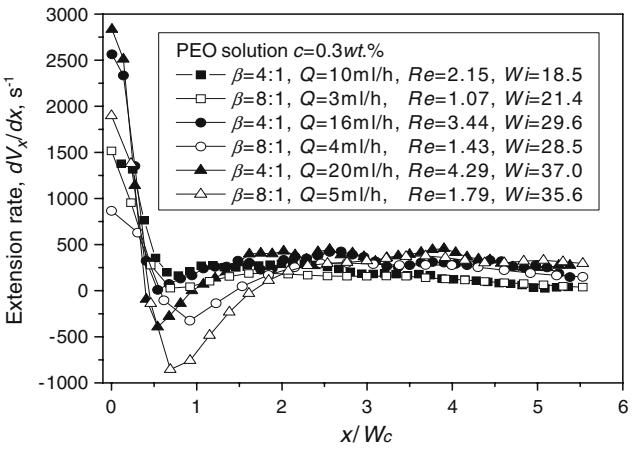

Fig. 12 Comparison of the profiles of the extensional deformation rate (calculated from the velocity profiles presented) between the 4:1 (No. 1) and 8:1 (No. 2) contraction micro-channel flows at comparable Weissenberg numbers

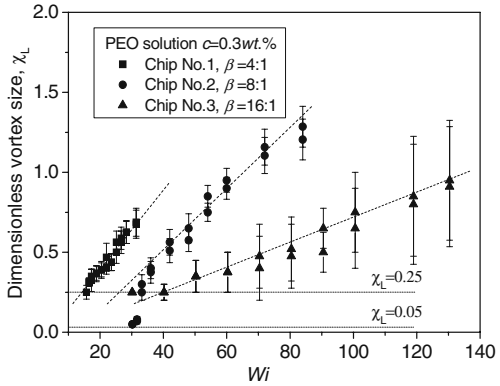

Fig. 13 Plot of the dimensionless vortex size χ_L against *Wi* for the 0.3 wt.% PEO solution flow in the upstream of 4:1, 8:1 and 16:1 contraction micro-channels (Nos. 1–3)

Characterization of vortex size

Following the convention adopted in White and Baird (1988), the dimensionless vortex size is defined as $\chi_L = L_v/w_u$, where L_v is the distance between the detachment point of the salient corner vortex and the concave corner. This is plotted against *Wi* in Fig. 13 for the 0.3 wt.% PEO solution flow in the three different contraction geometries ($\beta = 4{:}1, 8{:}1$ and 16:1). In the 4:1 contraction flow, the vortex size grows roughly linearly with increasing *Wi* over the whole range of flow rate. In the 8:1 and 16:1 contraction flow, however, there is a lip vortex flow regime for $28 < Wi < 32$. By the definition, the dimensionless vortex size remains quite small in this flow regime. However, in the corner vortex flow regime ($Wi > 32$), there is a nearly linear relationship between the dimensionless vortex length and *Wi*. The error bar increases with the contraction ratio because the vortex becomes less symmetric and less stable with higher contraction ratios, as illustrated in Fig. 8. For comparable Weissenberg numbers, the vortex size found in this work is larger than that reported by Rodd et al. (2005). This is probably due to either the different polymer samples or the different downstream geometric conditions.

Effect of the narrow channel length

As shown in Table 1, three of the 8:1 contraction micro-channels have different narrow channel lengths, L_c = 20 mm (No. 2), 4 mm (No. 4) and 0.4 mm (No. 5), respectively. Similar non-linear fluid dynamics have been observed in micro-channels Nos. 4 and 5 as were described previously for the No. 2 micro-channel (see Fig. 9). The transition from the steady viscoelastic to lip vortex flow regime is at $Wi \approx 23$, which is slightly lower than what is observed in the No. 2 micro-channel ($Wi \approx 28$). However, the effects of the narrow channel length on the vortex growth and the pressure drop over the contraction geometry are significant.

Figure 14 plots the dimensionless vortex size against *Wi* for the 0.3 wt.% PEO solution flow in three 8:1 contraction micro-channels. For equal *Wi*, the longer the length of the narrow channel, the larger is the vortex size. In the Nos. 2 and 4 micro-channel, the dimensionless vortex size grows approximately linearly with *Wi*. Whereas in the No. 5 micro-channel, the linear growth of the vortex size with *Wi* only holds in the low *Wi* range ($Wi < 60$). At higher *Wi*, the vortex size gradually reaches a plateau.

As shown in Fig. 15a, the dependence of the extensional rate profiles along the centerline on *Wi* for the 0.3 wt.% PEO solution flow in the No. 5 micro-channel resembles the key features of those described in Section "Velocity measurement and evaluation of local extensional deformation rate" for the other 8:1 contraction micro-channels. However, at high flow rates ($Wi > 60$) the profiles do not change very much. This is consistent with the gradual saturation of the vortex growth in the No. 5 micro-channel shown in Fig. 14. The extensional rate profiles for the 0.3 wt.% PEO solution flow in three micro-channels (Nos. 2, 4 and 5) at comparable Weissenberg number in the corner vortex flow regime are plotted in Fig. 15b. The shorter the length of the narrow channel, the higher the extensional deformation rate at the contraction throat and the shallower the compression valley is. The vortex size is also reduced.

Figure 16a shows the steady-state pressure drop ΔP_{12} over the upstream and downstream for 0.3 wt.% PEO solution and water flow in micro-channels Nos. 2, 4 and 5 for a range of flow rates. The pressure drop of the PEO solution increases linearly in Newtonian-like flow regime for all the flow geometries.

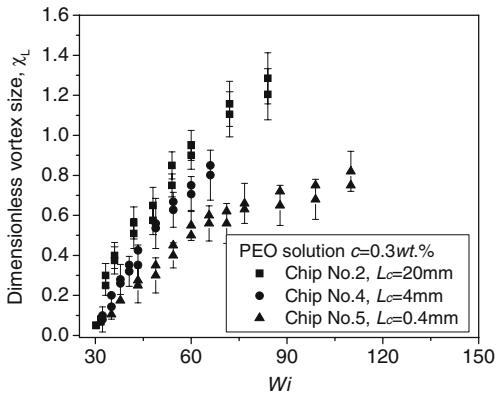

Fig. 14 Plot of the dimensionless vortex size χ_L against *Wi* for the 0.3 wt.% PEO solution flow in the 8:1 contraction micro-channels with L_c = 20 (No. 2), 4 (No. 4) and 0.4 mm (No. 5), respectively

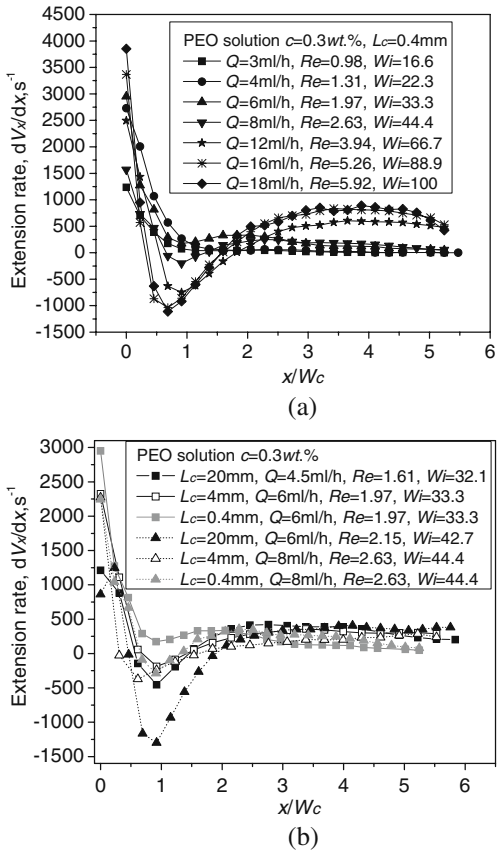

Fig. 15 **a** The profile of extensional deformation rate along the centreline of the No. 5 micro-channel and **b** comparison of the extensional rate profiles along the centreline between 8:1 contraction micro-channels (Nos. 2, 4 and 5) at comparable Weissenberg numbers

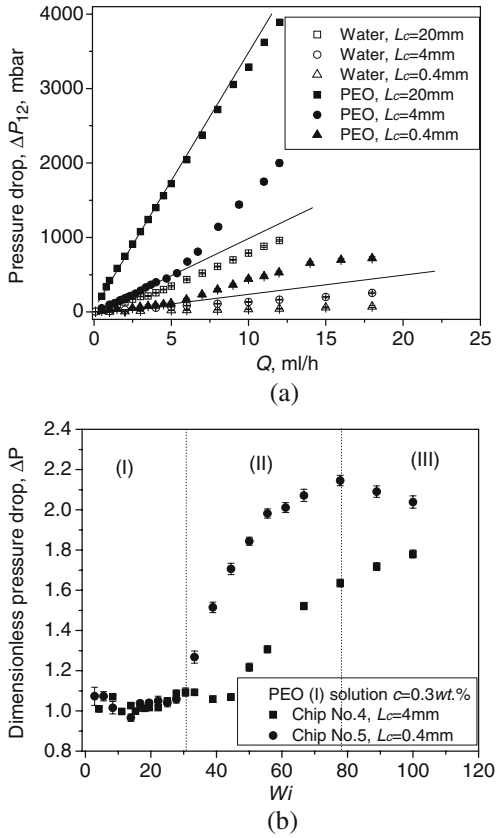

Fig. 16 Pressure drop between the upstream and downstream for 0.3 wt.% PEO solution flow in micro-channels Nos. 2, 4 and 5: **a** $\Delta P_{12} \sim Q$ and **b** $\Delta P' \sim Wi$

A method to extract the meaningful excess pressure drop in the contraction–expansion flow with long narrow channel (such as No. 2) has been suggested by Li et al. (2011). Here, a simplified method is used to reveal the effects of the narrow channel length on the pressure drop between the micro-channel Nos. 4 and 5.

By fitting the pressure drop curves in Fig. 16a at low flow rates, the gradient $d(\Delta P_{12})/dQ$ (when $Q \to 0$) for the flow in micro-channel Nos. 4 and 5 could be obtained. The pressure drop is normalised as $\Delta P = \Delta P12/\left(Q \cdot d\left(\Delta P_{12}\right)/dQ\right)$. The dimensionless pressure drop is plotted against *Wi* in Fig. 16b, which clearly shows three regimes. In regime (I), including the Newtonian-like, steady viscoelastic flow and lip vortex flow regime, $\Delta P \to 1$ as $Wi \to 0$, and the value of the dimensionless pressure drop fluctuates around unity. In regime (II), i.e. the corner vortex flow regime, ΔP increases rapidly with *Wi* and approaches a maximum value. ΔP measured in No. 5 micro-channel is higher than that in No. 4 micro-channel, and after the maximum point, it decreases as *Wi* increases in regime (III), probably due to the finite overall strain that can be imposed on polymer molecules through such a contraction–expansion flow. The finite strain is limited by the contraction ratio and the length of the narrow channel. The shape of the ΔP vs *Wi* curve is similar to that reported in Rodd et al. (2005, 2007). As the length of the narrow channel increases, the curve ΔP vs *Wi* curve shifts to higher *Wi* range and the maximum value of ΔP decreases. The contribution of shear components from the narrow channel to the overall ΔP becomes significant. The alternative method (Li et al. 2011) to extract the excess pressure drop should be used.

Conclusions

The effects of the contraction ratio and the narrow channel length on non-linear dynamics of semi-dilute polydisperse polymer solutions in 3-D shallow contraction–expansion flow geometry are studied by μ-PIV technique and pressure drop measurement. In the 4:1 contraction flow, symmetric and stable corner vortices are observed over a wide range of *Re* and

Wi. In the 8:1 and 16:1 contraction flow, the vortex dynamics initiates from a lip vortex and subsequently grows into a corner vortex as flow rate increases. Highly asymmetric and unstable flows are found in the 16:1 contraction flow. There is even coexistence of two vortices on one side of the upstream channel in high *Wi* flow, which has not been observed previously and is worthy for future study. As the contraction ratio implies the degree of Hencky strain to be imposed on polymer chains in the contraction flow, the elasticity number, defined by the dimensions of the narrow channel, is not sufficient to account for the effects of the contraction ratio (defined by the upstream channel width as well as the narrow channel width) on the non-linear evolution of flow patterns.

Although the flow patterns generated from the 8:1 contraction flow with different lengths of narrow channels share many common features, the effects of the narrow channel length on the vortex growth and the pressure drop over the contraction geometry are significant. Decreasing the length of the narrow channel, the *Wi* at which flow transition takes place from one regime to another effectively shifts to a lower value of *Wi*. At a comparable *Wi*, the vortex size is also reduced. Moreover, the long narrow channel ensures fully developed flow to be established in the narrow channel. This decouples the non-linear dynamics in the downstream expansion channel from the vortex dynamics in the upstream channel.

The excess pressure drop across the upstream and downstream regions is a sensitive quantity to characterize non-linear flow of polymer solution. Three flow regimes can be clearly identified from the excess pressure drop curves and correlated with the flow regime in term of the upstream vortex dynamics. In addition to the rheological properties of fluid, the flow geometry such as the contraction ratio, the aspect ratio and the length of the narrow channel can affect the vortex dynamics of polymer solution in the contraction–expansion benchmark flow, even under comparable *Wi*. These experimental results provide not only quantitative experimental data for validation of constitutive models and numerical simulations, but also useful guidance in the optimization of microfluidic design for high throughput characterization of viscoelastic fluids in microscopic flow.

Acknowledgements The authors would like to acknowledge the financial support of the Engineering and Physical Sciences Research Council (EP/E032699 and EP/E033091) and Linkam Scientific Instruments Ltd., and to thank Alfredo Lanzaro, Sunday Omowunmi and Joseph Dawes for their stimulating discussions, Colin Booth and Keith Nixon at the University of Manchester for their GPC analysis.

References

Aboubacar M, Matallah H, Webster MF (2002) Highly elastic solutions for Oldroyd-B and Phan-Thien/Tanner fluids with a finite volume/element method: planar contraction flows. J NonNewtonian Fluid Mech 103(1):65–103

Alves MA, Pinho FT, Oliveira PJ (2000) Effect of a high-resolution differencing scheme on finite-volume predictions of viscoelastic flows. J NonNewtonian Fluid Mech 93(2–3): 287–314

Alves MA, Oliveira PJ, Pinho FT (2004) On the effect of contraction ratio in viscoelastic flow through abrupt contractions. J NonNewtonian Fluid Mech 122(11):117–130

Alves MA, Pinho FT, Oliveira PJ (2005) Visualizations of Boger fluid flows in a 4:1 square-square contraction. AIChE J 51(11):2908–2922

Baloch A, Townsend P, Webster MF (1996) On vortex development in viscoelastic expansion and contraction flows. J NonNewtonian Fluid Mech 65(2–3):133–149

Binding DM (1988) An approximate analysis for contraction and converging flows. J NonNewtonian Fluid Mech 27:173–189

Binding DM, Walters K (1988) On the use of flow through a contraction in estimating the extensional viscosity of mobile polymer solutions. J NonNewton Fluid Mech 30(2–3):233–250

Boger DV (1987) Viscoelastic flows through contractions. Ann Rev Fluid Mech 19:157–182

Cable PJ, Boger DV (1978a) A comprehensive experimental investigation of tubular entry flow of viscoelastic fluids. Part I. Vortex characteristics in stable flow. AIChE J 24(5): 869–879

Cable PJ, Boger DV (1978b) A comprehensive experimental investigation of tubular entry flow of viscoelastic fluids. Part II. The velocity field in stable flow. AIChE J 24(6): 992–999

Cable PJ, Boger DV (1979) A comprehensive experiental investigation of tubular entry flow of viscoelastic fluids. Part III. Unstable flow. AIChE J 25(1):152–159

Cogswell FN (1972) Converging flow of polymer melts in extrusion dies. Polym Eng Sci 12(1):64–73

Devanand K, Selser JC (1991) Asymptotic behavior and long-range interactions in aqueous solutions of poly (ethylene oxide). Macromolecules 24(2):5943–5947

Evans RE, Walters K (1986) Flow characteristics associated with abrupt changes in geometry in the case of highly elastic liquids. J NonNewton Fluid Mech 20(11):11–29

Evans RE, Walters K (1989) Further remarks on the lip-vortex mechanism of vortex enhancement in planar-contraction flows. J NonNewtonian Fluid Mech 32(1):95–105

Groisman A, Enzelberger M, Quake SR (2003) Microfluidic memory and control devices. Science 300:955–958

Gulati S, Muller SJ, Liepmann D (2008) Direct measurements of viscoelastic flows of DNA in a 2:1 abrupt planar micro-contraction. J NonNewtonian Fluid Mech 155:51–56

Haward SJ, Odell JA, Li Z, Yuan XF (2010a) The rheology of polymer solution elastic strands in extensional flow. Rheol Acta 49(7):781–788

Haward SJ, Li Z, Lighter D, Thomas B, Odell JA, Yuan XF (2010b) Flow of dilute to semi-dilute polystyrene solutions through a benchmark 8:1 planar abrupt micro–contraction. J NonNewtonian Fluid Mech 165(23–24):1654–1669

James DF, Saringer JH (1982) Flow of dilute polymer solutions through converging channels. J NonNewtonian Fluid Mech 11(3–4):317–339

Li Z, Yuan XF, Haward SF, Odell JA, Yeates S (2011) Non-linear dynamics of semi-dilute polydisperse polymer solutions in microfluidics: a study of a benchmark flow problem. J Non-Newtonian Fluid Mech (in press)

McKinley GH, Raiford WP, Brown RA, Armstrong RC (1991) Nonlinear dynamics of viscoelastic flow in axisymmetric abrupt contractions. J Fluid Mech 223:411–456

Nigen S, Walters K (2002) Viscoelastic contractions flows: comparison of axisymmetric and planar configurations. J Non-Newtonian Fluid Mech 102(2):343–359

Omowunmi SC, Yuan XF (2010) Modelling the three-dimensional flow of a semi-dilute polymer solution in microfluidics—on the effect of aspect ratio. Rheol Acta 49(6): 585–595

Purnode B, Crochet MJ (1996) Flows of polymer solutions through contractions. Part 1: flows of polyacrylamide solutions through planar contractions. J NonNewtonian Fluid Mech 65:269–289

Quinzani LM, Armstrong RC, Brown RA (1994) Birefringence and laser-Doppler velocimetry (LDV) studies of viscoelastic flow through a planar contraction. J NonNewtonian Fluid Mech 52(1):1–36

Quinzani LM, Armstrong RC, Brown RA (1995) Use of coupled birefringence and LDV studies of flow through a planar contraction to test constitutive equations for concentrated polymer solutions. J Rheol 39(6):1201–1228

Rodd LE, Scott TP, Boger DV, Cooper-White JJ, Mckinley GH (2005) The inertio-elastic planar entry flow of low-viscosity elastic fluids in micro-fabricated geometries. J NonNewtonian Fluid Mech 129:1–22

Rodd LE, Boger DV, Cooper-White JJ, Mckinley GH (2007) Role of the elasticity number in the entry flow of dilute polymer solutions in micro-fabricated contraction geometries. J NonNewtonian Fluid Mech 143:170–191

Rothstein JP, McKinley GH (1999) Extensional flow of a polystyrene Boger fluid through a 4:1:4 axisymmetric contraction/expansion. J NonNewtonian Fluid Mech 86(1–2): 61–88

Rothstein JP, McKinley GH (2001) The axisymmetric contraction–expansion: the role of extensional rheology on vortex growth dynamics and the enhanced pressure drop. J NonNewtonian Fluid Mech 98(1):33–63

White SA, Baird DG (1988) Flow visualization and birefringence studies on planar entry flow behavior of polymer melts. J NonNewtonian Fluid Mech 29:245–267

Williams PR, Williams RW (1985) On the planar extensional viscosity of mobile liquids. J NonNewtonian Fluid Mech 19:53–80

Xue S, Phan-Thien N, Tanner RI (1998) Three dimensional numerical simulations of viscoelastic flows through planar contractions. J NonNewtonian Fluid Mech 74(1–3):195–245